Optical volumetric inspection of sub-20 nm patterned defects with wafer noise

Bryan M. Barnes*[a], Francois Goasmat[a], Martin Y. Sohn[a], Hui Zhou[a], András E. Vladár[a], Richard M. Silver[a], Abraham Arceo[b]
[a]Semiconductor & Dimensional Metrology Division, National Institute of Standards and Technology, 100 Bureau Drive MS 8212, Gaithersburg, MD, USA 20899-8212;
[b]SEMATECH North, 257 Fuller Road, Albany, NY USA 12203-3652

ABSTRACT

We have previously introduced a new data analysis method that more thoroughly utilizes scattered optical intensity data collected during defect inspection using bright-field microscopy. This volumetric approach allows conversion of focus-resolved 2-D collected images into 3-D volumes of intensity information and also permits the use of multi-dimensional processing and thresholding techniques to enhance defect detectability. In this paper, the effects of wafer noise upon detectability using volumetric processing are assessed with both simulations and experiments using the SEMATECH 9 nm node intentional defect array. The potential extensibility and industrial application of this technique are evaluated.

Keywords: wafer noise, defect inspection, volumetric processing, defect metrology, three-dimensional image processing

1. INTRODUCTION

Optical methods are instrumental for patterned defect inspection in semiconductor fabrication, as the quality of these measurements directly affect manufacturing yield. Optical imaging is inherently parallel and thus covers relatively large areas quickly compared to scanning techniques, leading to higher throughput. However, the International Technology Roadmap for Semiconductors (ITRS) shows that ever-decreasing sizes of features and spaces in these patterns have strained the capabilities of optical tools to differentiate between killer defects and false positives. The ITRS also reports that there are currently no known solutions for achieving desired processing speeds and capture rates [1]. In addition, it can be shown that as dimensions decrease, killer defects will eventually scatter light [2] as Mie scatterers, having intensities effectively proportional to d^6/λ^4 (where d is the diameter of the scatter and λ is the wavelength of light) exacerbating the ongoing challenge of maintaining a sufficient signal-to-noise ratio (SNR).

We have recently developed a new, three-dimensional volumetric defect inspection method for mitigating the effects of random noise while using the continuity of the defect to bolster defect detection [3,4]. Initially, we are utilizing the full three-dimensional scattered field using focus-resolved imaging; though not performed here, angle-resolved sampling of the three-dimensional scattered field can also be processed volumetrically. Optical images are collected and data analysis performed to yield (x,y,z) indexed volumes of reflected light intensity data. The goal of this method is to separate measured intensities due to defects from all other intensities. A brief review of the volumetric technique follows in the next section.

These other intensities, which can lead to false positives and/or large reduction of the signal-to-noise ratio, originate generally either from the instrument or from wafer noise, defined below. Examples of instrument-based sources of imaging noise include the shot noise of the charge coupled device (CCD), the stray light and glare within the optical columns, and intensity inhomogeneities across the field of view from misalignment, lens imperfections, aberrations, and laser speckle. These sources of error can be significant but are reduced as much as practicable through optical design and design of experiment. In our experiments, speckle is partially removed by using a rotating diffuser at the source plane while aberrations have been reduced through design optimization. Furthermore, systematic instrumental noise effects are largely mitigated by collecting "defect" and "reference" sets of images consecutively for differential analysis under nearly the same experimental conditions. These procedures, coupled with a volumetric approach that reduces the effects of random noise, permit a more thorough exploration of the effects of wafer-based intensity noise relative to the defect.

*bryan.barnes@nist.gov; phone 1 301 975-3947; fax 1 301 975-4299; www.nist.gov/pml/div683/grp02/om3dnm.cfm

Wafer noise is observed as scattering from the sample of interest due to its physical variations such as line edge roughness (LER) and line width roughness (LWR), as well as possible materials variation [2,5]. In many ways, the optical scattering behavior of wafer noise should mimic that of patterned defects. Wafer noise should be observable over an extended focal range. It should persist in differential imaging as the LER and LWR do not overlap between the "defect" and "reference" acquisitions. This paper studies the degree to which wafer noise qualitatively and quantitatively impacts defect detection using a through-focus volumetric approach with both simulated and experimental data presented.

2. OPTICAL THREE-DIMENSIONAL VOLUMETRIC PROCESSING

Although optical focus-resolved three-dimensional volumetric defect detection has been described in-depth elsewhere[2-3], it is important to reiterate the required steps to better explain the results presented. A schematic of the process is shown as Fig.1 using a simulation example. Sets of images of a defect are collected at various focus positions. These images are treated as *xy* slices of an *xyz* volume of intensities that can be constructed from these images, shown in Fig. 1(b). Repeating the process using a defect-free or defect-shifted sample yields a "reference" volume similar to the "defect" volume. Experimental volumes often require Fourier filtering and correlation [6], both performed in three dimensions. The reference and defect volumes can be subtracted to yield a differential volume as shown in Fig. 1(c). In this schematic, a strong signal from the defect is observable in the center as shown in the cut-out. For this illustration, random and correlated noise have been added to the difference volume after processing; elsewhere in this paper, wafer noise originates from the scattering off noisy samples and no additional imaging noise has been added. To derive Fig. 1(d), the differential data are converted to absolute values and thresholded using a minimum intensity creating several sub-volumes. By filtering the three-dimensional spatial extent of these sub-volumes, the scattering due to the defect can be identified in the center of Fig. 1(d), with the noise sub-volumes scattered all around.

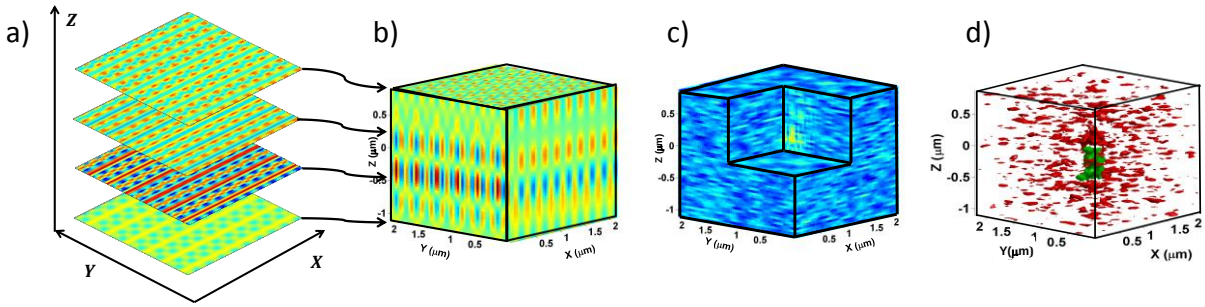

Figure 1. Schematic of three-dimensional volumetric processing. a) Images from a defect are collected or simulated through focus. b) These images can be transformed into a volume of intensity information. Likewise, a reference volume can also be obtained. c) The defect and reference volumes are subtracted yielding a differential volume. A cut-out shows the defect within. d) Intensity and spatial extent thresholding yields the large central sub-volume [green online] in the center due to a defect, the remaining sub-volumes are noise [red online].

Differential experimental images presented in Ref. 2 further illustrate this methodology. Due to wafer shifting to obtain the "reference" volume, there are two copies of the defect visible in each case below. Two elongated sub-volumes in Fig. 2 on the left are due to the presence of a defect. The remaining sub-volumes are noise. Compared to the data on the left in Fig. 2, the experimental results shown on the right in Fig. 2 were obtained using less light, structured illumination, and a die with imperfect patterning, as determined from scanning electron microscopy (SEM) images. Again, through intensity and spatial extent thresholding, the two copies of the defect can be identified.

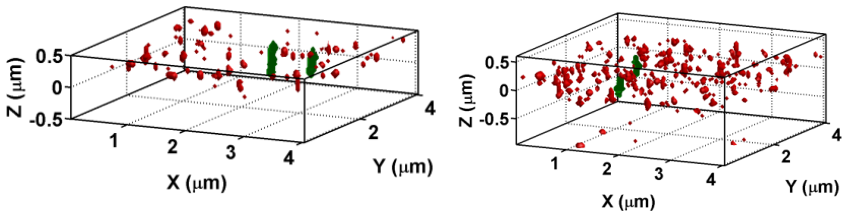

Figure 2. Two examples of volumetrically processed through focus differential images from Ref. [2]. The defect volumes can be visualized after thresholding, colored green online. Data subvolumes colored red online are noise.

The initial work, specifically Fig. 2, right, raised several key issues. Data from a die with imperfect patterning were collected using a different illumination configuration yielding less light. From such an experiment, it was unclear whether the added noise was due to an increase in wafer noise or was due to less light available at the sample. Empirically, the defect optical signature extended through a longer focal *z* range than the noise – could wafer noise be expected to have an extent in *z* as large as a defect? Two simulation studies are presented to compare the optical scattering behavior of samples with LER, LWR, and imperfections relative to the optical scattering from intentionally patterned defects. Experiments on a well-patterned die and the same imperfectly patterned die from Fig. 2, under the same illumination conditions, yield a systematic evaluation of wafer noise.

3. SIMULATION STUDIES WITH WAFER NOISE

Two separate simulation studies were performed, both based upon the SEMATECH 9 nm intentional defect array (IDA). In one study, LER was applied to the IDA design layout to determine the spatial extent of wafer noise and the extensibility of volumetric methods to 9 nm critical dimensions (CDs). For another study, structures on a patterned IDA wafer were measured using SEM and these images were transformed into inputs to the scattering simulation. This exercise allows a more realistic comparison to the experimental measurement as the inherent LER, LWR, and pattering imperfections of the IDA thus better represented in the simulation. In these studies, the primary concentration was on the "$\mathcal{B}x$" and "$\mathcal{B}y$" bridging defects which connect the line segments orthogonally as shown in Fig. 3.

Each study employs electromagnetic scattering simulations using a finite-difference time domain (FDTD) [7] solver at λ = 193 nm, the measurement wavelength. The intensity threshold for both simulation studies is four times the standard deviation of the absolute value of each differential image. Volumetric pixels (voxels) with intensities (I) above 4σ must next meet continuity requirements with other $I > 4\sigma$ voxels. Finally, a spatial extent threshold assesses the size of the smallest box – the "bounding box" – that would contain each sub-volume. The minimum bounding box for a defect sub-volume was set to 100 nm x 100 nm x 600 nm.

Both studies used the same defect metric and estimator for the signal-to-noise ratio. The defect metric here is the sum of the intensities in the defect sub-volume(s). The signal-to-noise (SNR) requires a more in-depth discussion. From one perspective, this volumetric data processing method optimally yields two distinct and separable data sets per differential volume: sub-volume(s) attributed to the defect, and sub-volume(s) attributed to the noise. An SNR from that perspective is ill-defined. The introduction of an intensity threshold complicates straightforward approaches to the calculation. Although Poline *et al.* have presented statistical treatments for combining spatial extent testing and peak intensity thresholding for assessing the risk of error in analyzing three-dimensional positron emission tomography (PET) images[8], we construct an estimate for the SNR consistent with the work of McCann *et al.* who presented several approaches to determining a SNR for magnetic resonance imaging with regions-of-interest [9]. The mean of the defect sub-volume(s), I_{defect}, is the signal, while the standard deviation across the noise sub-volume(s), σ_{noise}, is the noise, yielding

$$\boldsymbol{SNR \approx \frac{I_{defect}}{\sigma_{noise}}}. \tag{1}$$

This treatment will allow quantitative comparison among the data within a given simulation or experimental data set.

3.1 First Study: Adding LER to the GDS

This first study permits investigation of the extensibility of volumetric processing and the effects of wafer noise by applying a well-defined line edge roughness (LER) to the nominal design of the 9 nm node IDA through its Graphic Data System (GDS) file. This LER is characterized by its rms roughness, σ, and its correlation length, ξ. Simulation inputs were generated using a procedure laid out by Crimmins [5] for applying a correlation length to a random sequence. The correlation length is invoked using a target autocorrelation function,

$$\boldsymbol{f(x) = \xi^{1/2}\pi^{-1/4}\, e^{\frac{-x^2}{2\xi^2}}}. \tag{2}$$

This modified random sequence was added to the sides and ends of each line segment within the GDS file including the defect. Specifically, one randomization yielded an LER with (σ,ξ) for a defect-free reference while a separate randomization was used to generate LER with the same magnitude (σ,ξ) for the line arrays of the "*Bx*" and "*By*" defects. This process ensured a mismatch between the edge geometries of the reference and defect.

Initial values for the LER rms roughness was 0.65 nm (one standard deviation) with ξ = 8 nm. These values were derived from the ITRS, setting the LER comparable to current LWR (uncorrelated) while assigning ξ a more aggressive value that follows the 9 nm node [10]. The rms roughness could not be equally aggressive due to the computational requirements of the FDTD model to approximate LER at these length scales. An investigation for this effort was made to compare the scattering behavior due to FDTD grid size for a given LER rms roughness, evaluating σ = 0.65 nm using cubic grid sizes 0.75 nm to 2.25 nm. A second investigation varied the FDTD domain size from 1 x 3 unit cells (0.72 μm x 0.72 μm in *xy*) up to 4 x 12 unit cells (2.88 μm x 2.88 μm in *xy*). After evaluating tradeoffs among speed, accuracy, and computational capabilities, the domain size used here was 1 x 3 with a grid size of 1.125 nm, or 9/8 nm for these 9 nm node designs.

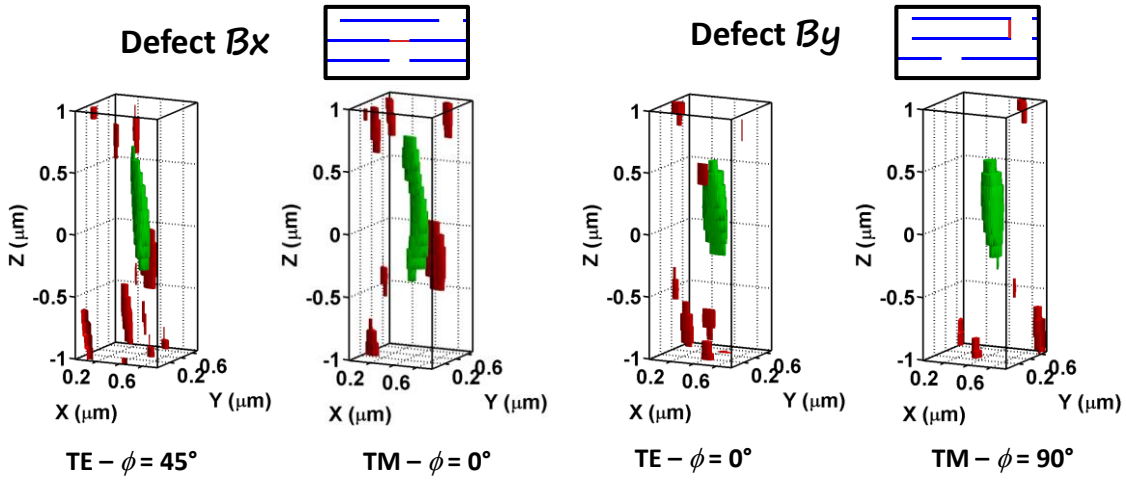

Figure 3. (top) Schematic representations of the "*Bx*" and "*By*" bridging defects. (bottom) Volumetric differential images of the two defects for the TE and TM polarizations at the stated azimuthal angle ϕ with polar angle θ = 21° from normal incidence.

The defect metric and SNR for the data in Fig. 3 are provided in Table 1. In each case, the defect is easily identified and separable from the noise. Quantitatively, the "*By*" bridge defect is relatively stronger than that for the "*Bx*" defect in either linear polarization. While some noise sub-volumes are present in the data, none persist through focus on par with the main defect optical scattering signal.

Table 1. Defect metric and signal-to-noise (SNR) estimate for the 9 nm node with σ = 0.65 nm.

	Bridge *Bx*		**Bridge *By***	
	TE – ϕ = 45°	TM – ϕ = 0°	TE – ϕ = 0°	TM – ϕ = 90°
Def. Int. > 4σ	2238	3500	8585	7979
SNR	11.5	9.3	18.9	16.6

Thus as σ = 0.65 nm LER left the defect signal largely unperturbed, these simulations can be used as a baseline to evaluate the effects of doubling and tripling the rms roughness to further assess the role of LER on defect detectability. Figures 4 and 5, defects "*Bx*" and "*By*" respectively, display portions of the unit cell and defect from the GDS, with LER wafer noise increasing from left to right. These figures illustrate potential difficulties in defect detection with increased LER. In Fig. 4 for defect "*Bx*", visual comparison of the σ = 0.65 nm LER versus the others shows that the

defect is not correctly identified at σ = 1.35 nm and σ = 1.90 nm. For "$\mathcal{B}y$", the defect is identified at both σ = 0.65 nm and σ = 1.35 nm, consistent with its stronger signal in Table 1.

Table 2 shows the defect metrics, SNR, and $I > 4\sigma$ intensity thresholds for the data in Figs. 4 and 5. The SNR for the "$\mathcal{B}y$" defect decreases between the σ = 0.65 nm and σ = 1.35 nm cases. For the "$\mathcal{B}x$" defect, the σ = 1.35 nm and σ = 1.90 nm values for the defect metric and SNR are shown but italicized (and colored red, online) to demonstrate that these obtained values do not correspond to an actual defect signal.

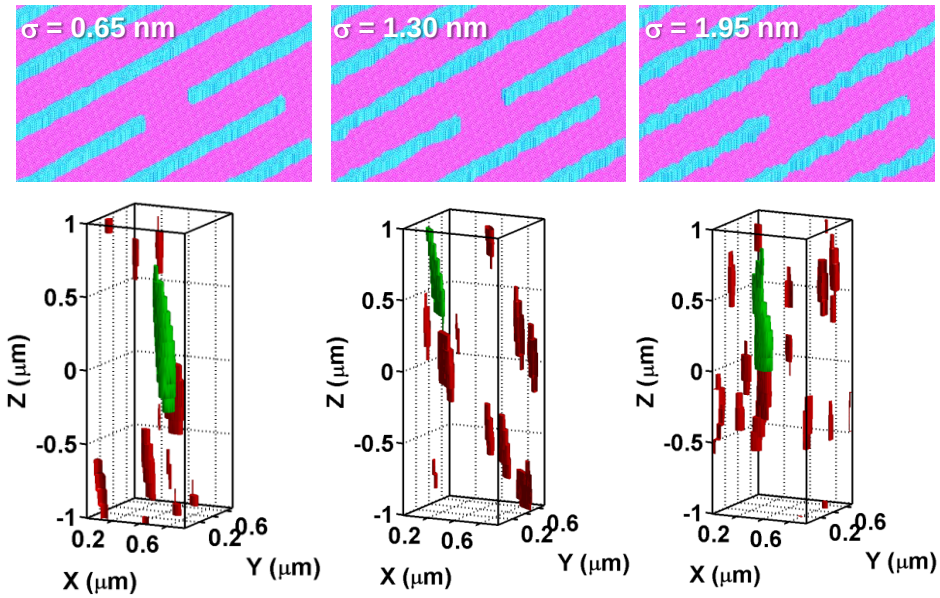

Figure 4. Differential volumetric analysis for the $\mathcal{B}x$ defect using TE polarization, $\theta = 21°$, $\phi = 45°$ for three different LER rms roughnesses. The defect is only correctly identified at $\sigma = 0.65$ nm.

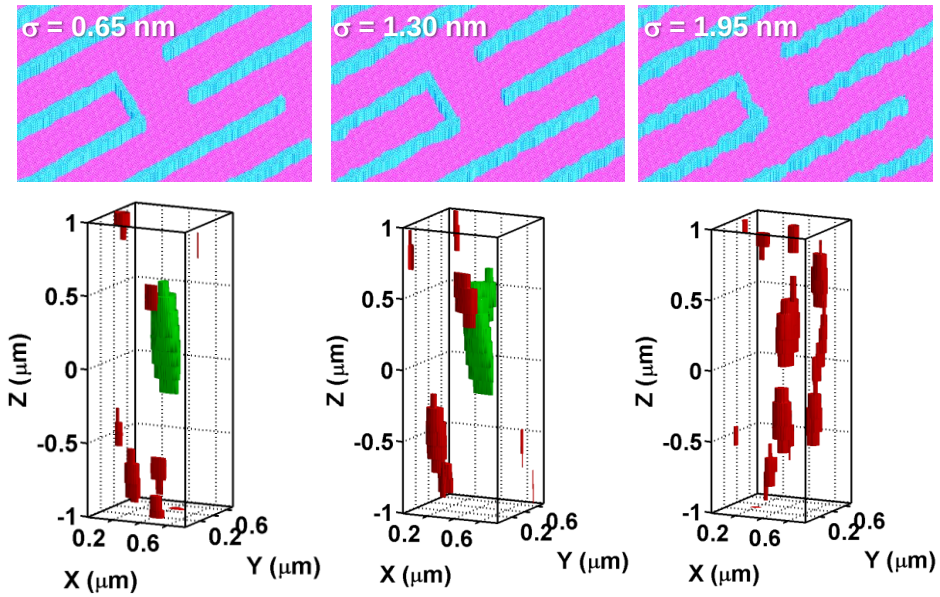

Figure 5. Differential volumetric analysis for the "$\mathcal{B}y$" defect using TE polarization, $\theta = 21°$, $\phi = 0°$ for three different LER rms roughnesses. The defect is correctly identified at $\sigma = 0.65$ nm and $\sigma = 1.35$ nm.

Table 2. Defect metric, signal-to-noise (SNR) estimate, and intensity threshold with the rms roughness, σ, of the LER increasing from 0.65 nm to 1.95 nm.

	Bridge *Bx*			Bridge *By*		
	0.65 nm	1.30 nm	1.95 nm	0.65 nm	1.30 nm	1.95 nm
4σ Intensity	0.021	0.022	0.041	0.069	0.089	0.066
Def. Int. > 4σ	2238	*552*	*1693*	8585	10669	*N/A*
SNR	11.5	*15.7*	*15.2*	18.9	9.0	*N/A*

This simulation study confirms that wafer noise can be detected volumetrically along with the defect for low LER rms roughness values. Increased LER may reduce the SNR, while large LER will likely eliminate detectability. More data are required to provide additional qualitative and quantitative analysis. While this study is useful for developing the extensibility of volumetric processing, achieving a fuller understanding of the experimental data presented in Fig. 2 and in Section 4 may be better achieved through a simulation study of the LER, LWR, and imperfections as observed on this sample on interest.

3.2 Second study: SEM data in the FDTD

The second simulation study compares the wafer noise from the SEMATECH 9 nm node IDA using SEM data to define the simulation geometry. Instead of relying upon the nominal design from the GDS file as modeling input, the simulation was based entirely upon SEM images acquired from two specific dies on the IDA chosen for their patterning quality. For each die, images of the "*A*" defect (nominally an island defect), the "*Bx*" and "*By*" defects, and the "*J*" defect (a line break) were collected then correlated and cropped to show 3 x 4 unit cells with the defect near the center of the image. A fifth cropped image for each die was taken from the periphery of the image of the "*By*" defect as a reference defect-free pattern. These 10 images in all were converted using intensity thresholding from greyscale SEM images to binary masks. For these normalized SEM images, this threshold was 0.35 and thus the apparent critical dimensions fed into the FDTD are slightly larger than would be expected from a more traditional 50 % threshold. The binary mask in Fig. 6(a) comes from the "well-patterned die" while Fig. 6(b) shows a mask derived from the "imperfect die". These two separate dies offer variations in LER, LWR, and line fidelity. The sidewalls of the simulated structures were assumed to be normal. Perspective views of the defects appear in Fig. 7.

From these masks, the LER, LWR, and line fidelity were computed from the middle 80 % of the patterned lines. The LER varied among defects within each die. Unplanned imperfections and line breaks in the imperfectly patterned die contributed to the approximate 1 nm increase in LWR relative to the well-patterned die. The LWR may be difficult to visualize in the figures below as the pixel resolution is nominally 2.48 nm/pixel. The continuity of the well-patterned die is nearly 100 % but only 98 % or more for targets on the imperfectly patterned die.

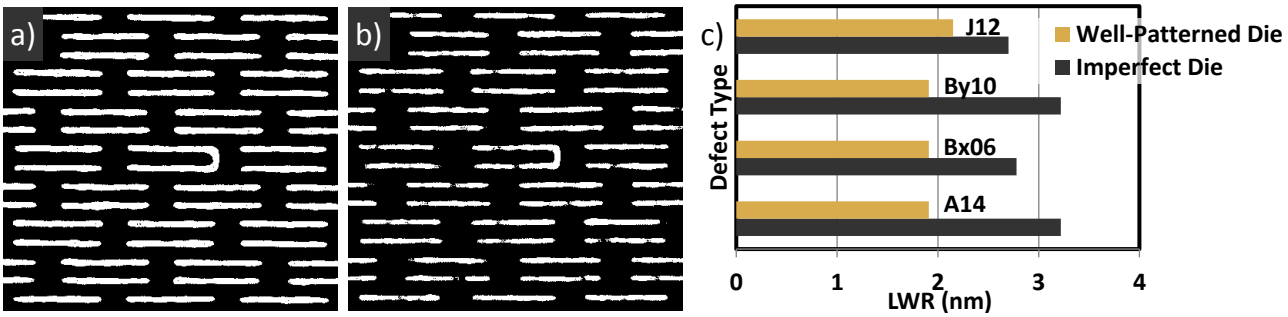

Figure 6. Comparisons of the simulation inputs for the "well-patterned die" versus the "imperfectly patterned die." a) The "*By*" defect binary mask for the well-patterned die. b) The "*By*" defect binary mask for the imperfectly patterned die. c) Line width roughness (LWR) calculated for the "*A*", "*Bx*", "*By*", and "*J*" defects. For this paper, the analysis is restricted to the "*Bx*", "*By*" defects.

The 2.48 nm SEM pixel resolution provided the lower limit for the cubic FDTD grid size and enabled many more FDTD simulations to be performed relative to the first simulation study in which a 1.125 nm grid size was used. The polar angle was varied from $\theta = 11°$ to 45° with the azimuthal angle ranging from $\phi = 0°$ to 90°. This simulation covers one quadrant of the conjugate to the back focal plane of the objective lens in the National Institute of Standards and Technology (NIST) 193 nm microscope. If these samples were two-fold symmetric, these simulations would be sufficient for simulating the full-field illumination available on the microscope. As the sample is nearly two-fold symmetric, concentration on this quadrant alone yields an approximation. Assuming incoherent illumination and Köhler illumination, several plane wave simulations have been combined to simulate finite-aperture monopole illumination for the TE and TM polarizations in Fig. 7 for the two dies and two defects of interest.

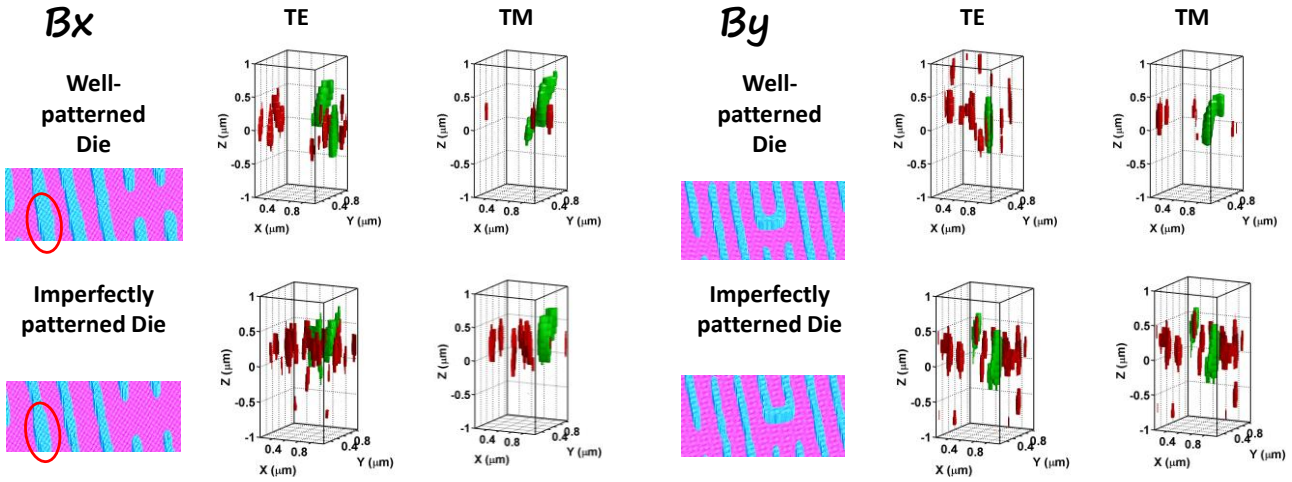

Figure 7. Differential volumetric analysis of the scattering from two dies and two defect types from the 9 nm node IDA using two polarizations.

Qualitatively, there are more defect sub-volumes from the scattering from the imperfect die than from the well-patterned die, confirming that wafer effects can be expected to manifest themselves as wafer noise. Defect sub-volume(s) were identified for each of these eight possible combinations of die, defect type, and polarization, with less noise apparent in the TM polarization. The defect metric, SNR, and the critical dimensions of the defects simulated are shown in Table 3.

Table 3. Defect metric and SNR comparing two die of differing patterning quality, with the critical dimension of the defect simulated using FDTD. Though based on SEM measurement, the defect critical dimensions (CDs) are fixed inputs to the model; the specific SEM intensity threshold used overestimates the CD compared to the SEM CD measurements in Table 4.

	Well-patterned die				Imperfectly patterned die			
Defect	Bridge *Bx*		Bridge *By*		Bridge *Bx*		Bridge *By*	
Polarization	TE	TM	TE	TM	TE	TM	TE	TM
Def. Metric	1278	1912	707	1459	953	1335	1222	1489
SNR	13.1	17.6	15.5	18.9	9.5	10.8	12.4	13.9
Defect CD	28 nm		26 nm		26 nm		20 nm	

Quantitatively, the well-patterned die consistently demonstrates a higher intensity defect metric and SNR relative to the imperfect die. The defect metric and SNR are larger for the TM polarization than the TE polarization. Also, the defect metric and the SNR both show that the "*By*" defect is more easily detected than the "*Bx*" defect. These trends will be evaluated experimentally in Section 4.

4. EXPERIMENTAL VOLUMETRIC DEFECT DETECTION

4.1 Comparison of dies on the SEMATECH 9 nm IDA

Simulation studies have shown that extra wafer noise is to be expected in the three-dimensional volumetric analysis of samples with LER and specifically for the imperfectly pattered die. These trends must be confirmed using experimental data. Previously, direct comparison between the imperfectly patterned die and another well-pattered die was hampered by substantially different illumination conditions. In this experiment, "$\mathcal{B}x$" and " $\mathcal{B}y$" defects are measured on two dies on the 9 nm IDA using bright-field illumination using the NIST 193 nm Microscope [11]. The full-field effective illumination numerical aperture (NA) is annular due to a catadioptric objective and ranges from 0.12 NA to 0.74 NA. As discussed in the Introduction, the "defect" and "reference" volumes are collected sequentially and instrumentation noise effects should be largely mitigated, allowing investigation of the wafer noise.

As shown in Fig. 8, there is more wafer noise from the imperfectly patterned die than from the well-patterned die. In Fig. 8(b), two copies of the "$\mathcal{B}y$" defect are clearly identified with the noise sub-volumes mostly confined to a narrow *z* range. For the same defect on the imperfect die shown in Fig. 8(d), two false positives have been detected and the noise sub-volumes approximately 250 nm in *z* extent. For "$\mathcal{B}y$" the *xyz* extents of the defect signals differentiate the defect from the noise. Contrast this with Figs 8(a) and 8(c), where the labeled noise sub-volumes often are positioned in the same *z* range as the intentional defect. From the simulation studies, LER effects did not produce such wafer noise. A number of the noise sub-volumes in Figs 8(c) also have copies due to the shift between the "defect" and "reference" image, thus it is likely that these are unintended defects, such as the line breaks observed by SEM in Fig. 6(b), with intensity noise on par with the scattering from the "$\mathcal{B}x$" defect. Similar events are less readily observed in Fig. 8(d) due to the relatively large intensity of the "$\mathcal{B}y$" defect.

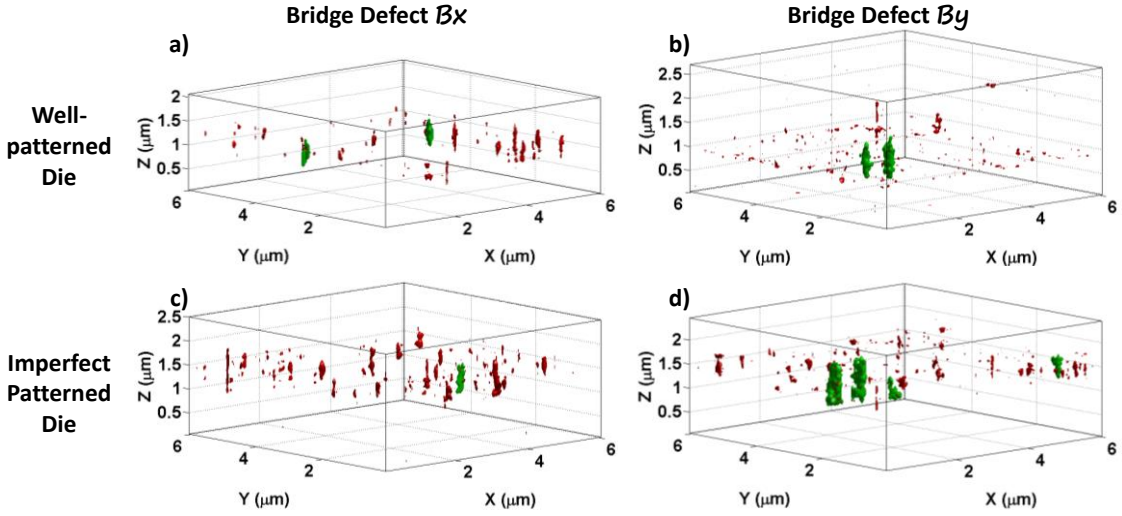

Figure 8. Experimental differential volumetric defect detection comparing the measured intensities from the imperfectly patterned die versus a well-patterned die on the 9 nm IDA. Thresholds are consistent for a given defect: the "$\mathcal{B}x$" defect was analyzed using a 7σ intensity threshold with a 160 nm x 160 nm x 550 nm spatial extent, the "$\mathcal{B}y$" defect was analyzed using a 6σ intensity threshold with a 160 nm x 160 nm x 700 nm spatial extent. In both cases, wafer noise is larger on the imperfectly patterned die.

The experimental defect metric and SNR are provided in Table 4. For these experiments, the defect metric is the mean intensity per pixel in the defect sub-volume(s). As opposed to the simulation studies, volumetric processing of imperfectly pattered die quantitatively teases out the defect signals well. The differences in the defect metrics and SNR for the two "$\mathcal{B}x$" defects are minimal. Values for the two "$\mathcal{B}y$" defects indicate a greater detectably for the imperfectly patterned die.

Table 4. Experimental defect metric and SNR comparing two dies of differing patterning quality, with the critical dimension of the defect as measured using SEM. SEM CD values are averages of the defect's width as measured between 25 % and 75 % of its length using a 0.42 normalized intensity threshold. SEM uncertainties are 1σ values (k=1).

	Well-patterned die		Imperfectly patterned die	
Defect	Bridge *Bx*	Bridge *By*	Bridge *Bx*	Bridge *By*
Polarization	X	Y	X	Y
Def. Metric	0.065	0.020	0.059	0.035
SNR	12.5	11.9	10.6	16.1
CD (SEM)	28 ± 3 nm	21 ± 3 nm	23 ± 2 nm	19 ± 2 nm

4.2 Extensibility of Through-Focus Techniques

While these experiments demonstrate the utility of volumetric processing for samples with wafer noise, the added data acquisition required to assemble such volumes suggests that this approach is impractical for full-time manufacturing process control. Volumetric process may best be applied intermittently, for example to identify a likely focal position where defects may be identified with little noise, or applied after conventional single-focus inspection to measure a marginally flagged defect more closely before defect review. In developing this methodology, the time required for a measurement was not optimized and the data set at left in Fig. 9 is comprised of 47 different *z* slices. In the center and right panels of Fig. 9, the *z* resolution is reduced to evaluate the effectiveness of volumetric methods with less data.

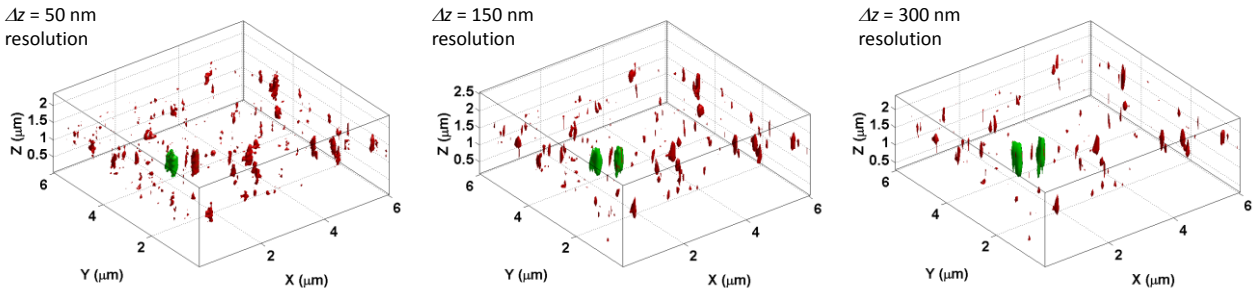

Figure 9. Experimental differential volumetric defect detection as the *z* resolution is reduced from left to right as shown. Although three-dimensional filtering and interpolation was performed at the highest *z* resolution, the intensity and spatial filtering was performed for each new *z* resolution.

Varying the *Δz* resolution from *Δz* = 50 nm to *Δz* = 300 nm in steps of 50 nm, the number of required slices was reduced from 47 to 8, with each iteration having a SNR comparable to the SNR of the highest resolution with only the *Δz* = 200 nm case (not shown) yielding a false positive. Otherwise, only the two copies of the defect were identified. Volumetric analysis with limited data sets may be optimal for integrating the advantages of this approach with the necessities of high-volume manufacturing.

5. CONCLUSIONS

Volumetric processing of focus-resolved images can be used to isolate defects in noisy data, as capturing images through focus not only finds an optimal focus for observing defectivity but also provides additional correlated data. Two-dimensional treatments of the data cannot fully utilize this information. Wafer noise due to the LER, LWR, and variations in the sample may similarly yield correlated data. The two simulation studies show that increased LER is likely to obscure the presence of the defect and that the imperfectly patterned die on the SEMATECH 9 nm IDA would yield lower SNR, but the *z* extent of the noise would not be as large as observed for the defect. In experimental measurements, noise sub-volumes did extend through the focal range similarly to the intentional "*Bx*" defect but this wafer noise is likely due to actual imperfections in the pattering and not changes in LER or LWR. Further evaluation showed that only a minimal number of *z*-slices may be required to implement this technology in industrial practice.

REFERENCES

[1] International Technology Roadmap for Semiconductiors, "2012 tables, Yield Enhancement," <http://www.itrs.net/Links/2012ITRS/2012Tables/Yield_2012Tables.xlsx> (2012).

[2] Crimmins, T. F.,"Defect metrology challenges at the 11nm node and beyond," Proc. SPIE 7638, 76380H (2010).

[3] Barnes, B. M., Sohn, M. Y., Goasmat, F., Zhou, H., Silver, R. M. and Arceo, A., " Enhancing 9 nm node dense patterned defect optical inspection using polarization, angle, and focus," Proc. SPIE 8681, 86810E (2013).

[4] Barnes, B. M., Sohn, M. Y., Goasmat, F., Zhou, H., Vladár, A. E., Silver, R. M. and Arceo, A., "Three-dimensional deep sub-wavelength defect detection using λ = 193 nm optical microscopy," Opt. Express 21, 26219-26226 (2013).

[5] Crimmins, T. F., "Wafer noise models for defect inspection," Proc. SPIE 7971, 79710E (2011).

[6] Evangelidis, G. D. and Psarakis, E. Z., "Parametric image alignment using enhanced correlation coefficient maximization," IEEE Trans. Pattern Anal. Mach. Intell. 30, 1-8 (2008).

[7] Taflove, A., "Application of the finite-difference time-domain method to sinusoidal steady-state electromagnetic-penetration problems," IEEE Trans. Electromagn. Compat. EMC-22, 191-202 (1980).

[8] Poline, J. B., Worsley, K. J., Evans, A. C., and Friston, K. J., "Combining Spatial Extent and Peak Intensity to Test for Activations in Functional Imaging," Neuroimage 5, 83–96 (1997).

[9] McCann, A. J., Workman, A., and McGrath, C., "A quick and robust method for measurement of signal-to-noise ratio in MRI," Phys Med Biol. 58(11), 3775-90 (2013).

[10] International Technology Roadmap for Semiconductiors, "2012 tables, Lithography," <http://www.itrs.net/Links/2012ITRS/2012Tables/Litho_2012Tables.xlsx> (2012).

[11] Sohn, Y. J., Quintanilha, R., Barnes, B. M., and Silver, R. M., "193 nm angle-resolved scatterfield microscope for semiconductor metrology," Proc. SPIE 7405, 74050R (2009).